Batteries & Supercaps

Research Article
doi.org/10.1002/batt.202300107

Chemistry
Europe
European Chemical
Societies Publishing
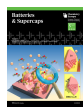
Regulating Zinc Deposition via Zincophilic 2D-Cu$_2$Te as the Current Collector to Suppress Dendrite Formation toward High Performance Aqueous Zinc-Ion Batteries

Ming-Hsuan Tsai$^+$,[a] Tuan-Yue Lin$^+$,[a] Tian-Shun Su,[a] Guan-Min Chen,[a] Yu-chen Liu,[b, c, d, e, f] and Yu-Ze Chen*[a, g]

In this study, we synthesized standing 2D δ-Cu$_2$Te flakes (δ-CTFs) via a facile post-tellurization process, which served as the current collector to accommodate zinc (Zn) for AZIBs. These flakes exhibited low nucleation overpotential and low interfacial impedance, facilitating the plating/stripping of Zn ions. Interestingly, the hydrophilicity and standing structure of δ-CTFs guided the electrodeposited Zn to laterally grow on the surface of δ-CTFs, effectively suppressing Zn dendrite formation. The Zn@δ-CTFs anode exhibited a long-term cycling duration of 510 hours in a symmetric cell, which is far superior to previous reports. Even under high current density of 10 mA cm^{-2}, the anode was able to perform stably with a cycle life of 110 hours. The machine learning model was exploited to predict the effective charge value, discovering that Zn migrated in Cu$_2$Te were subject to the larger driving force of migration under applied field. Finally, the Zn@δ-CTFs//MnO$_2$ full battery exhibited excellent rate-dependent capacity and maintained a capacity of 100 mAh g^{-1} after 1000 cycles at a current density of 1 A g^{-1}, without Zn dendrite formation. This research provides a new strategy for regulating Zn deposition to address dendrite issues toward long lifespan AZIBs.

Introduction

Lithium-ion batteries (LIBs) have been at the forefront of battery technology due to their high output voltage (3.2–3.7 V),

[a] M.-H. Tsai,$^+$ T.-Y. Lin,$^+$ T.-S. Su, G.-M. Chen, Prof. Y.-Z. Chen
Department of Materials Science and Engineering
National Cheng Kung University
Tainan City 70101 (Taiwan)

[b] Prof. Y.-c. Liu
Department of Mechanical Engineering
National Cheng Kung University,
Tainan City 70101, (Taiwan)

[c] Prof. Y.-c. Liu
Hierarchical Green-Energy Materials (Hi-GEM) Research Center
National Cheng Kung University
Tainan City 70101 (Taiwan)

[d] Prof. Y.-c. Liu
Program on Smart and Sustainable Manufacturing Academy of Innovative
Semiconductor and Sustainable Manufacturing
National Cheng Kung University
Tainan City 70101 (Taiwan)

[e] Prof. Y.-c. Liu
Program on Semiconductor Packaging and Testing Academy of Innovative
Semiconductor and Sustainable Manufacturing
National Cheng Kung University
Tainan City 70101 (Taiwan)

[f] Prof. Y.-c. Liu
Core Facility Center
National Cheng Kung University
Tainan City 70101 (Taiwan)

[g] Prof. Y.-Z. Chen
Program on Key Materials
Academy of Innovative Semiconductor and Sustainable Manufacturing
National Cheng Kung University
Tainan City 70101 (Taiwan)
E-mail: yzchen@gs.ncku.edu.tw

[$^+$] These authors contributed equally to this work.

Supporting information for this article is available on the WWW under
https://doi.org/10.1002/batt.202300107

high energy density (460–600 Wh kg^{-1}), and low self-discharge loss. However, the scarcity of lithium, as well as the Li dendrite growth and flammability of organic electrolytes, have raised concerns over their safety.[1] Hence, scientists put much effort on developing substitutes for a long-term reliable battery in the near future. Recently, aqueous rechargeable batteries have emerged as a promising option for portable energy-carrier devices due to their non-flammability and non-toxic electrolyte, promising the safety of utilization.[2] Among various metal demonstrated as anode in aqueous batteries, zinc (Zn) as anode has displayed intriguing properties, such as high volumetric capacity of 5855 mAh cm^{-3} and high earth abundance.[3,4]

Unfortunately, aqueous Zn-ion batteries (AZIB) face significant challenges, including dendrite growth at the Zn anode and side reactions, similar to LIBs.[5] Due to the the low redox potential (−0.76 V vs. standard hydrogen electrode (SHE)) of Zn, the H$_2$ generation was inevitable, leading to unstable Zn flux during deposition and resulting in perpendicularly dendritic Zn growth caused by the "tip effect". The dendritic Zn becomes "immobile" during stripping, which known as "dead Zn" and reducing reversibility and Coulombic efficiency.[6,7] Moreover, along with repeatedly cycling plating/stripping process, dendritic Zn were likely penetrated through the separator, resulting in the short circuit and the corrosion of Zn anode, sacrificing the lifespan of AZIB.[8] Therefore, in order to address the as-stated problems, a great variety of strategies toward the improved reliability and stability of batteries had been proposed. Material design strategies focus on stabilizing the Zn stripping/plating process from the different aspect: i) in-situ construction of artificial protecting layer on Zn by adding dimethyl sulfoxide (DMSO) into Zn(TFSI)$_2$ electrolyte.[9] ii) The

Batteries & Supercaps

Research Article
doi.org/10.1002/batt.202300107

Chemistry
Europe

European Chemical
Societies Publishing

artificial protecting layer coating on the Zn metal. To develop an artificial protecting layer on Zn anode, the basic concept of preventing Zn anode from dendrite growth and side reactions was able to regulate the Zn deposition and accelerate the Zn^{2+} transfer kinetics. However, the thickness of artificial coating layers occupied non-negligible volume occupation, hindering from the light-weighted portable batteries.[10–13] iii) The surface modification of Zn, such as texturing the grain orientation toward (002) which possesses the low surface energy of 0.02 eV$Å^{-2}$, assuring the Zn plated steadily on the (002) plane. Hence, the strategy of controlling the grain orientation was exposed the plane (002) as much as possible.[14,15] Furthermore, the commercial Zn foil was conventionally used as the anode for AZIB, but Zn utilization rate (ZUR) which was the percentage of Zn effectively involved in the stripping/ plating process was low (less than 5%).[16] Hence, to develop a suitable current collector to accommodate Zn would be an efficient way to improve ZUR as well as reducing the waste of Zn resource. By far, there are several reports of developing a suitable current collector for Zn. One approach is to prepare a 3D-porous substrate such as Cu,[17] Sn[18] and Cu–Zn alloy[19] achieved by the chemical etching process for serving as collector to accommodate the Zn ions during the plating/stripping process, improving ZUR by allowing more of the Zn ions to be stored and involved in the process. However, there is still room for improvement in the lifespan of the symmetric cell, and still challenging to perform under high current density.

The family of copper chalcogenides (Cu_2X, where X=S, Se, Te) demonstrated their versatility in the optical, electrical and electrochemical properties due to the tunable stoichiometry and diverse crystal structures. Cu_2S and Cu_2Se possessed intriguing properties including the high carrier mobility and narrowed band gap ranging from 1.8 to 2.4 eV, rendering them as potential anodes for lithium/sodium ion battery and solar energy harvesting.[20–22] Cu_2Te is a kind of superionic conductor due to the liquid-behavior Cu cations transports, exhibiting the metallic electrical transport with higher hole concentration up to 10^{21}–10^{22} cm^{-3} which was superior to that of Cu_2S and Cu_2Se.[23] Recently, the layered-structure of Cu_7Te_4 and Cu_2Te had successfully synthesized, proving the extraordinary properties of the excellent catalytic and interesting green photoluminescence, dragging much attention for the thermoelectric, electrochemical applications and semiconductor devices. As for the energy storage, Cu_2Te nanocubes served as the cathode for Li/$LiPF_6$/$Cu_{2-x}Te$ battery exhibited the longer lifespan over other cooper chalcogenides due to the heavy Te atoms enabling the tolerance of volume expansion during Li^+ charge/discharge process. To the best of our understanding, it is the first time to exploit 2D Cu_2Te flakes as the current collector for aqueous rechargeable battery toward the dendrite-free anode.

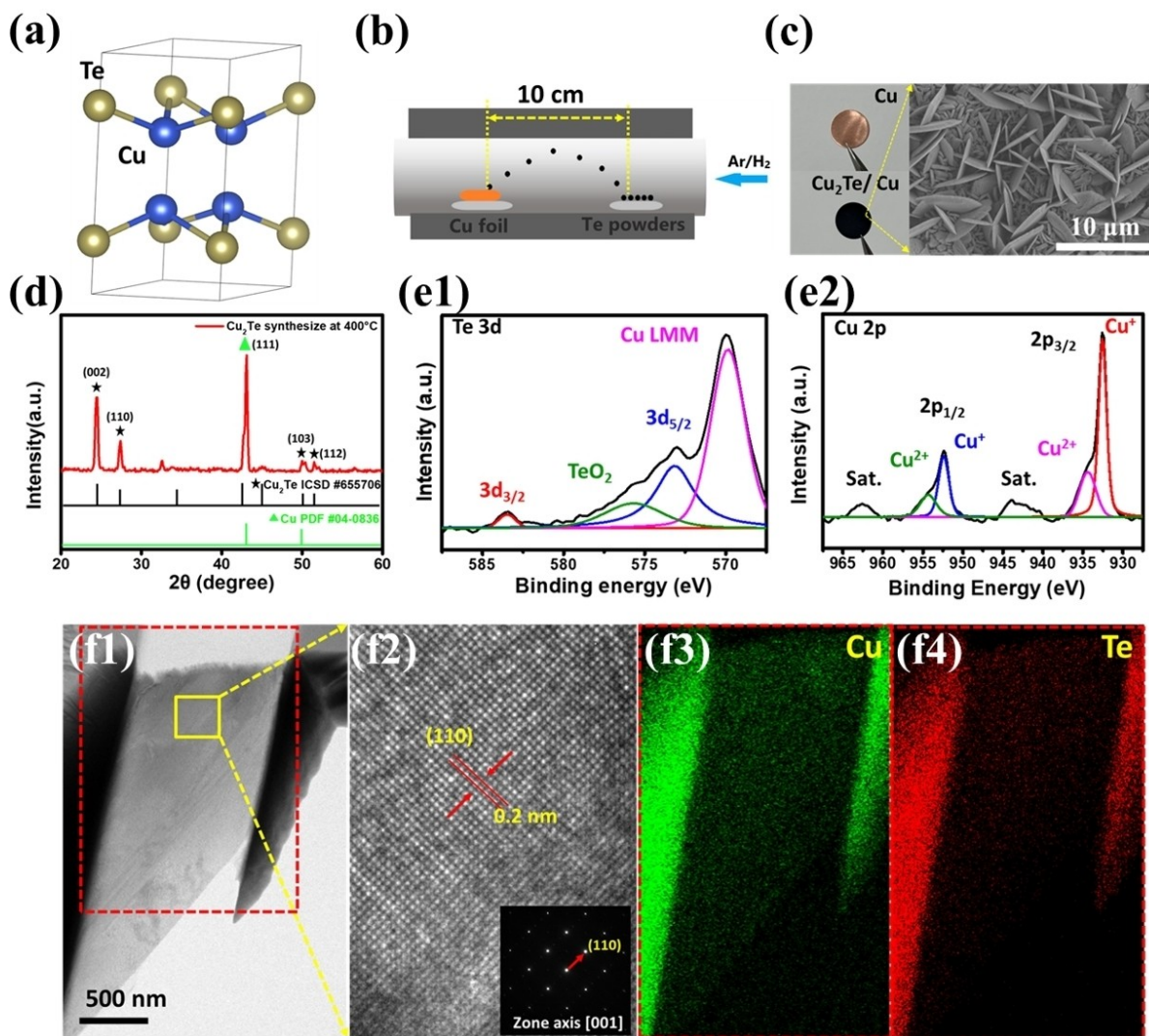In this study, standing δ-Cu_2Te flakes (δ-CTFs) were synthesized by post-tellurization of Cu foil. The morphology of δ-CTFs was found to be sensitive to growth parameters such as temperature and pressure, indicating a narrow window for growing standing flakes. The δ-CTFs were then utilized as the current collector for demonstrating AZIB. We found that when Zn was electrodeposited on the standing δ-CTFs, their 3D

structure guided the lateral Zn deposition along the surface, effectively suppressing dendritic growth. Finally, the full cell was demonstrated by coupling with MnO_2 as the cathode, exhibiting excellent rate dependence and long-term stability of 1000 cycles while maintaining 100 mAhg^{-1} and 100% Coulombic efficiency.

Results and Discussion

δ-Cu_2Te crystallizes in the hexagonal structure with the space group of P6/mmm ($a=b=$0.423 nm, $c=$0.729 nm, ICSD #655706) (Figure 1a). The Cu_2Te nanosheet was synthesized through the post-tellurization process conducted in the horizontal furnace, in which the Te powders were placed in the upstream region and copper foil (Cu) placed in the downstream region where was 10 cm away from Te powders (Figure 1b). After the tellurization process at 400 °C for 60 min, the color of Cu foil apparently changed from bright to dark, attributed to the standing 2D flakes with the layer thickness of 200 nm homogeneously distributed on copper foil confirmed by scanning electron microscopy (SEM), as shown in Figure 1(c). The crystallinity of Cu_2Te was characterized by X-ray diffraction (XRD), exhibiting the characteristic peaks at approximately 24.5°, 27.4°, 50° and 51.5° corresponding to the plane of (002), (110), (103) and (112) which were in well agreement with the standard card (ICSD #655706) (Figure 1d). In order to understand the bonding information of Cu_2Te, the X-ray photoelectron spectroscopy (XPS) analysis was exploited to analyze the chemical state of Cu and Te, respectively. The spectrum of Te 3d showed two peaks of Te $3d_{3/2}$ at 583.1 eV and $3d_{5/2}$ at 573.2 eV, respectively. In addition, a weak signal of TeO_2 at 575.7 eV peak was detected, and the XRD-induced Auger signal of Cu LMM at 568.6 eV also observed (Figure 1 (e1)). Figure 1(e2) displays the spectrum of Cu 2p, presenting two pairs of peaks at 954.3 (Cu^{2+} oxidation state) and 952.4 eV (Cu^+ oxidation state) of Cu 2p1/2 and 934.2 (Cu^{2+} oxidation state) and 932.1 eV (Cu^+ oxidation state) of Cu 2p3/2 with two satellite peaks at 963.5 and 943.6 eV.[24] In order to reveal the atomic structure of δ-Cu_2Te, transmission electron microscopy (TEM) was also performed. Prior to the TEM observation, the sample was prepared by focused ion beam (FIB) (Figure 1 (f1)). A high-resolution TEM image exhibits the distinguishable atomic arrangement, and the lattice spacing of 0.2 nm corresponded to (110) plane of Cu_2Te, which was consistent with the XRD results (Figure 1 (f2)). Inset displayed the selected area electron diffraction (SAED) pattern with clear diffraction spots, proving the high crystallinity. Figure 1(f3 and f4) shows the energy-dispersive X-ray spectroscopy (EDS) mapping imaegs of Cu and Te in the Cu_2Te flakes, exhibiting high uniformity of element distribution.

A intriguing properties of Cu_2Te was the complex phase transision corresponding to the different temperature and the unique atomic structures were responsible for the distinctive electrical and thermal property. Nevertheless, the influence of the different phase on the electrochemical properties have not reported yet. In the order to investigate the influence of

Batteries & Supercaps

Research Article
doi.org/10.1002/batt.202300107

Chemistry Europe
European Chemical
Societies Publishing

Figure 1. a) Atomic model of δ-Cu_2Te. b) Schematics of the synthesis of δ-Cu_2Te through the post tellurization process of Cu. c) Comparison of the photos of Cu foil and after through the post tellurization process. SEM images of Cu through the post tellurization process, presenting the standing flakes. d) XRD patterns of δ-Cu_2Te. XPS spectra of e1) Te 3d and e2) Cu 2p. f1) Low magnification TEM images and f2) high-resolution TEM images of single δ-Cu_2Te flakes, and the corresponding composition mapping results of the elements f3) Cu and f4) Te.

parameters on the morpology and atomic structures of Cu_2Te, the substrate temperature and process pressure were systematically studied. Figure 2 (a1–a5) displays the evolution of morphology with growth temperature increasing from 300 to 700 °C at the fixed pressure of 10 torr, obviously which was highly relevant to the resulting morphology of Cu_2Te from 2D flakes to thin film growth. When the temperature set to 300 °C, no formation of flakes were found due to the insufficient thermal energy triggered the reaction of Te (melting point: 449.5 °C) and Cu (Figure 2a1). Nevertheless, if the temperature increased to 400 °C, the standing δ-CTFs sucessfully formed with the width of 5 μm (Figure 2a2). In order to verify the possible growth mechanism, the lattice mismatch between two different materials is needed to be considered.[25] Considering the less lattice-mismatched heteroepitaxy, the (002) plane of δ-Cu_2Te is energy-perferentially seeded on the (111) plane of Cu due to the moderate lattice-mismatched (δ < 4%), thus result-

ing in the standing 2D growth (Figure S1). If the temperature set to 500 °C, the resulting flakes turned to wider and thicker with the increasing populations, attributed to the feedstocks of Te vapor increased (Figure 2a3). If the process temperature kept to 600 °C, the flakes begun to stack with each other (Figure 2a4). Interestingly, once the temperature was 700 °C, the flakes vanished and the film with large grains formed instead, implying that the growth model changed from flakes to the film growth (Figure 2a5). It is worth noting that the Cu_2Te synthesized at 700 °C underwent the phase transformation from δ phase (hexagonal phase) to ε phase (cubic Cu_2Te and cubic $Cu_{3.6}Te_2$) confirmed by the XRD examination (Figure S2).[26] Next, the morphology of Cu_2Te is also sensitive to the pressure control. Therefore, Cu_2Te synthesized at 400 °C with different pressures were designed for the exploration of the pressure effect on the morphology evolution. Figure 2 (b1–b5) exhibits a series of images evolved with the pressure
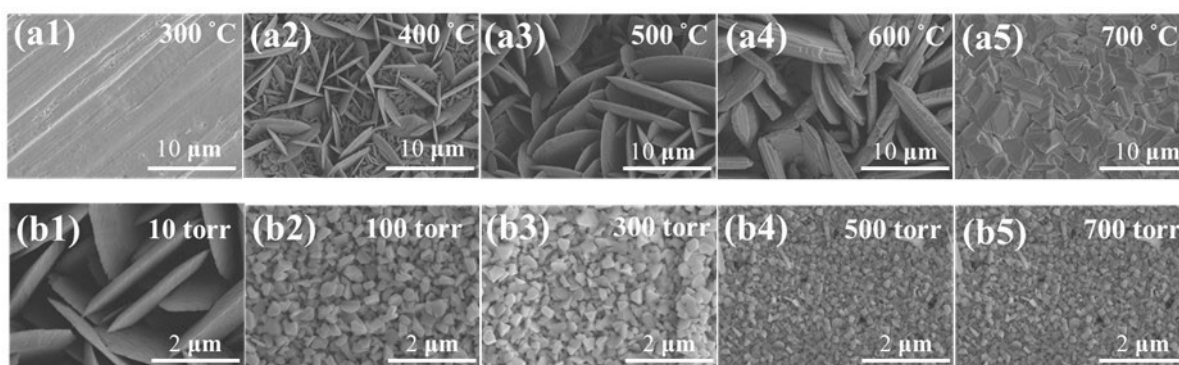
Figure 2. Morphology evolution of Cu_2Te varied with process temperature at a1) 300 °C, a2) 400 °C, a3) 500 °C, a4) 600 °C, a5) 700 °C. And with pressure at b1) 10 torr, b2) 100 torr, b3) 300 torr, b4) 500 torr, b5) 700 torr.

increasing. Note that the formation of the standing 2D flakes were dominated at 10 torr, implying the surface reaction of Cu surface was the rate-limited step. Whereas, if the pressure was set to 100–700 torr, the dense and finely polyhedrons of Cu_2Te were observed at the surface of Cu, speculated that the collisions between the Te vapor and Cu increased, giving rise to more nucleation sites. Moreover, Te powders with different amounts were carried out to achieve an optimal morphology. To analyze the effect of the precursor amount on the morphology of δ-Cu_2Te, SEM was employed as shown in Figure S3. Clearly, Cu_2Te synthesized using different amounts of Te powders exhibited the morphology evolution from finely polyhedrons to the standing flakes. When 3 or 5 mg of Te powders was employed, the tiny polyhedrons with a few flakes on the surface of Cu were revealed by SEM observation due to the limited Te feedstocks. When the amount of Te powders increased to 20 mg, a great number of larger flakes were observed on the surface of Cu, attributed to the suffcient Te feedstocks provided.

Next, the standing δ-CTFs was chosen as a current collector to electroplate Zn using 1 M $ZnSO_4$ and 0.5 M Na_2SO_4 as electrolyte at the current density of 20 mA cm^{-2} for 30 min (denoted as Zn@Cu_2Te). Firstly, to evaluate the stability of Cu_2Te flakes in the acid electrolyte, the corrosion test was conducted by immersing Cu_2Te into 2 M $ZnSO_4$ and recorded by *ex-situ* SEM observations over 21 days. Encouragingly, the appearance of flakes was still distinctive even throughout the 21 days (Figure S4), indicating the chemically-inert property in the harsh environment, proving its promising candidate as the current collector for AZIB. Figure 3(a1–a3) illustrates the process of the Zn deposition on δ-CTFs. After the electroplating process completed, the morphology of standing flakes was still distinguished, and noted that there was no formation of Zn dendrite on the surface (Figure 3a2), suggesting the protrusions of the standing flakes did not induce the "tip" effect to interfere the Zn deposition. In contract, the bare Cu also applied for electrodepositing Zn, as shown in Figure S5. Remarkbly, the Zn deposition on Cu foil was uneven in where some area revealed the color of bottum Cu. On contrary, after the electrodeposition of Zn on δ-CTFs, the sample was completely covered with Zn displaying the uniform gray color.

As confirmed by the zoom-in SEM image of single flakes (Figure 3a3), the Zn was perferentially deposited on the surface of flakes rather than at the edge of flakes, and owing to the 3D structure the Zn deposition was guided to the lateral expansion, implying that the synergistic effect of the zincophilic property itself with the 3D structure greatly and effectively suppressed the formation of the vertical Zn dendrite. In addition, based on aforementioned results, the morphology of Cu_2Te realized in this work varied from flakes, particles, and film by controlling the temperature and pressure. Hence, Cu_2Te particles and film were chosen to be electrodeposited Zn with different time for comparison. Figure S6(a1–a4) displays the evolution of surface morphology of Cu_2Te flakes varied with deposited time. Remarkably, Zn was deposited along the surface of flakes, implying the lateral growth of Zn was governed. Figure S6(b1–b4) display the evolution of surface morphology of Cu_2Te particles varied with deposited time. Apparently, it was found that the dense dendrites appeared only after 10 min electrodeposition of Zn and the density of dendrites elevated with the increasing time. Figure S6(c1–c4) exhibit the evolution of surface morphology of Cu_2Te film varied with deposited time. The dendrites vigorously grew at the first 10 min and the following growth direction was gradually toward the Z-axis, resulting in the vertical protrusions. Next, the hydrophobic property of Zn metal resulted in the uneven Zn plating, and thus the surface modifications to ameliorate the wettability is the crucial step toward the long-term stability and the practical usage.[27] The contact angle measurement was conducted for bare Cu, δ-CTFs and Zn@δ-CTFs, respectively (Figure 3b1–b3). The surface of bare Cu exhibited hydrophobic property with the contact angle up to 93.15°. By contract, the contact angle of δ-CTFs significantly decreased to 9.66°, exhibiting the highly wettable surface property, which was remarkably improved compared with previous report.[28] After electrodeposited Zn onto δ-CTFs, the contact angle slightly increased to 39.42°, still exhibited the hydrophilic property. Briefly, the great improvement in wettability of the standing δ-CTFs was ascribed to the synergistic effect of the nature hydrophilicity and the nanostructure at the surface, expected to be benefitial to the Zn ion electrodeposition. To invesigate the phase-dependent electrochemical
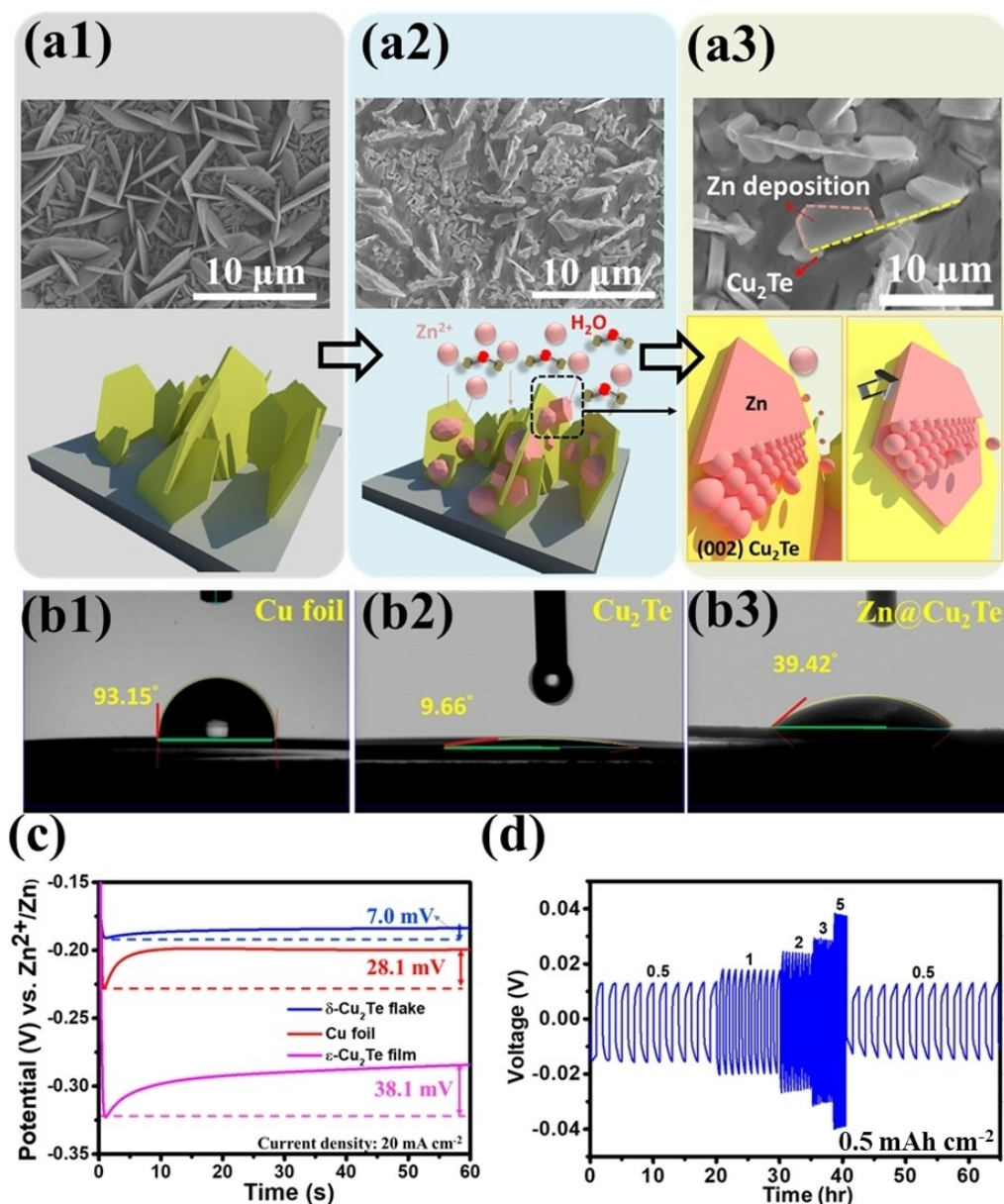
Figure 3. Electrodeposition of Zn on δ-Cu$_2$Te flakes. a1) The standing δ-Cu$_2$Te flakes served as the current collector. a2) SEM images of Zn electrodeposited on the δ-Cu$_2$Te flakes. a3) Magnified SEM images of few flakes, proving the Zn was laterally deposited. Results of Contact angle measurements for b1) Cu foil, b2) δ-Cu$_2$Te and b3) Zn@δ-Cu$_2$Te, respectively. c) Nucleation examination of the Zn electrodeposition on δ-Cu$_2$Te flakes (blue line), Cu foil (red line) and ε-Cu$_2$Te film (pink line), respectively. d) The rate performance of Zn@δ-Cu$_2$Te flakes symmetric cells at various current densities from 0.5 to 5 mA cm^{-2} with the capacity of 0.5 mAh cm^{-2}.

behavior was of interest of the energy strorage research, especially on the rechargeable batteries.[29,30] Hence, to further examine the zincophilic property of Cu$_2$Te with different phase, the nucleation overpotential of Zn deposition on ε-Cu$_2$Te films, δ-CTFs and Cu foil were conducted for comparison (Figure 3c). According to the previous reports, Cu had been reported to be the suitable current collector for the deposition of Zn due to the strong binding energy with Zn.[31] As expected, the results for Cu (red line) exhibited the low value of 28.1 mV, which was lower than that of ε-Cu$_2$Te (38.1 mV). On contract, the results for δ-CTFs yielded the considerable small value of 7.0 mV, suggesting that zincophilic sites on δ-CTFs enable to achieve

uniform Zn deposition. Remarkbly, such low nucleation potential was superiour to the previous report of using activated carbon cloth (ACC)[32] and brass mesh as current collectors.[33] In order to examine the surface stability of Zn@δ-CTFs during the cycling Zn stripping/plating process, the symmetric cells were assembled for the examination at the different step of current density from 0.5, 1, 2, 3, 5 mA cm^{-2} with the capacity of 0.5 mAh cm^{-2}. With the increasing the current density, the voltage hysteresis became gradually larger due to the gradient of Zn concentration enhanced. However, our Zn@δ-CTFs symmetric cells yielded the highly-dependent rate capability, indicating the high surafce stability (Figure 3d).

Batteries & Supercaps

Research Article
doi.org/10.1002/batt.202300107

Chemistry Europe
European Chemical
Societies Publishing

In contrast, the Zn@Cu symmetric cells were also assembled for comparison. Remarkbaly, it exhibited the unstable rate-dependent capacity at varied current densities (Figure S7). Figure 4(a1) exhibited the cycling perfromance of Zn@δ-CTFs (blue line) and Zn@Cu (red line) symmetric cells at the current density of 1 mA cm^{-2} and the capacity of 0.5 mAh cm^{-2} (ZUR = 5%). Remarkbly, Zn@δ-CTFs symmetric cells displayed the stable voltage output up to 400 h with the small voltage hysterisis of 47 mV. In contract, bare Cu as the current collector displayed the abrup voltage drop at 30th cycles, implying the internal
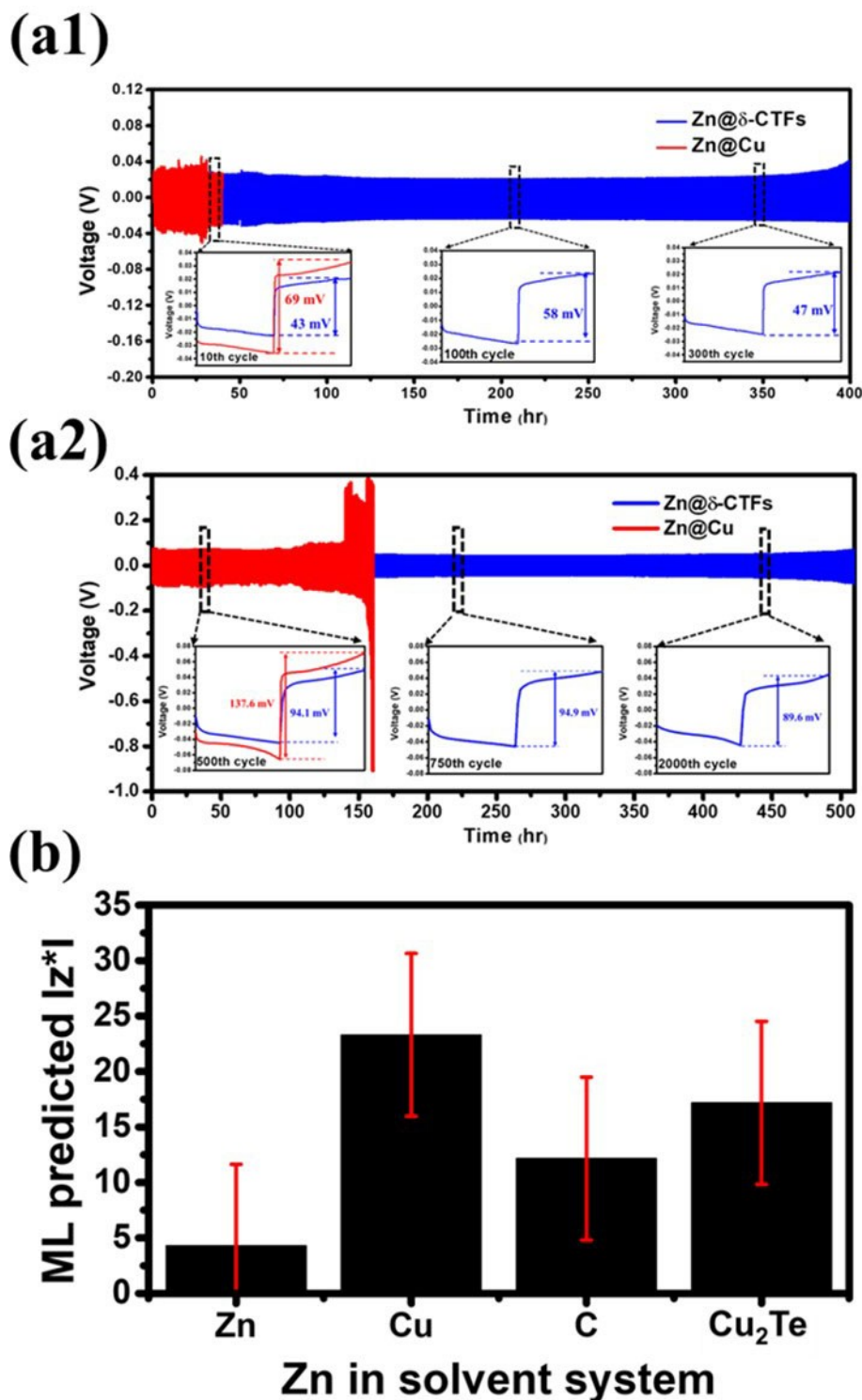
Figure 4. Cycling performance of symmetric batteries for Zn@δ-Cu$_2$Te and Zn@Cu, respectively. a1) under the current density of 1 mA cm^{-2} and capacity of 0.5 mAh cm^{-2} (ZUR = 5%) and a2) under the current density of 5 mA cm^{-2} and capacity of 0.5 mAh cm^{-2} (ZUR = 10%). c) Effective charge value of the impurity Zn in pure Zn, Cu, C and Cu$_2$Te as host predicted by machine learning model.

short curcuit caused by the Zn dendrite formation and side reactions.[34] Next, to demonstrate a higher ZUR, the Zn electrodeposited at the 10 mA cm^{-2} for 30 min and followed by the examination at the current density of 5 mA cm^{-2} and capacity of 0.5 mAh cm^{-2} (resulting in ZUR = 10%). Impressively, Zn@δ-CTFs symmetric cells stably performed with the voltage hysteresis of 89.6 mV and lasted for 510 hours. As for the bare Cu, the voltage exhibited the divergence at around 110 hours and failed at 150 hours (Figure 4a2). Moreover, even under ultra high current density 10 mA cm^{-2} and capacity 1 mAh cm^{-2}, Zn@δ-CTFs symmetric cells was still enabled to operate up to 115 hours (Figure S8), implying the structural rigidity of δ-CTFs can accommodate the volume change caused by the vigorous Zn stripping/plating. By demonstrating outstanding performance in terms of cycling stability and voltage hysteresis, δ-CTFs appear to be a promising candidate as a current collector for AZIB. In addition, the appearance of 2D flakes have a beneficial effect on the electrochemical performance, which could be due to several features, such as the increased surface area of the flakes, allowing for more efficient ion transfer, and excellent hydrophilicity and zincophilicity, advancing the Zn stripping/plating. Due to the complex atomic structures of Cu$_2$Te, it was necessary to clarify the impact of the δ phase and appearance of 2D flakes on the electrochemical performance. Based on the previous results of the phase and morphology controlled by the growth parameters, we selected δ-Cu$_2$Te particles and ε-Cu$_2$Te films to assemble the symmetric cells for comparison at the current density of 1 mA cm^{-2} and 0.5 mAh cm^{-2} (Figure S9). The δ-Cu$_2$Te particles symmetric cell exhibited the small voltage hysterisis of 44 mV, which was slightly smaller than that of δ-Cu$_2$Te flakes cell, However, the voltage started to fluctuate and eventually failure at around 120 h due to the Zn dendrites and side reactions. Meanwhile, the initial voltage of ε-Cu$_2$Te films symmetric cells were 80 mV with maintaining the stable cycling performace around 220 h, which obviously underperformed than others, reasonably ascribed to the larger nucleation potential (38.1 mV), indicating that the δ phase effectively alleviate the polarization possibly due to the less mismatch with Zn and the low nucleation potential. In contrary, the δ-CTFs symmetric cells delivered the outstanding cycling performance up to 400 h with the small voltage hysteresis, attributed to the synergistic effect of zincophilicity of Cu$_2$Te and the design of the 3D structure. Table 1 shows a comparison

of relevant research on the 3D-structured current collector for accommodating Zn in AZIB anodes based on the current density/capacity and cycling number.[31,33,35–41] Based on the reported performance, the cycling number was still far from practical usage, and more importantly, cycling tests conducted at high current densities remained challenging. However, our δ-CTFs as the anode demonstrated improved cycling performance for up to 510 hours. Even more impressively, under a high current density of 10 mA cm^{-2}, it still maintained long-term stability for up to 115 hours.

Machine learning (ML) has been applied to accelerate the development of clean energy technologies.[42] Here, we firstly emploited the ML model to predict the effective charge responsible for the fast migration of Zn in Cu$_2$Te host, which is likely due to the electric field-assisted effect. When an electric field is applied, species tend to migrate under the influence of the field, which is known as the electromigration (EM) effect.[43] The driving force behind the electromigration (EM) effect is a synergistic combination of the electron wind force and the external electric field force. The electron wind force is generated by the flow of electrons in the material, while the external electric field force is applied from outside the material. The synergistic effect of these two forces can result in the migration of species in the material.[44] To prove this perspective, we employed the machine learning (ML) approach to calculate the effective charge of the impurity Zn in pure Zn, Cu, C and Cu$_2$Te as a host. The calculate results present as shown in Figure 4(b), where the effective charge values are shown in absolute value to provide a more intuitive representation of the driving force scale. The error bar in the figure represents the model error, which was determined to be 7.84. From the results of calculation, the effective charge of Zn in pure Zn host exhibited the lowest effective charge value, which was close to that of Zn in pure C host. In contract, the effective charges of Zn in pure Cu and that in Cu$_2$Te display a relative higher value. The above results indicate that qualitatively or semi-quantitatively the driving force of Zn migration under applied electric field in pure Zn host was the lowest. Zn impurity in Cu2Te host, on the other hand, shows a larger driving force of migration under applied field. Based on the findings, we speculate that the electric field may play a vital role in understanding the fast migration of Zn in Cu$_2$Te.

Table 1. A list of the cycle life under the different current density and capacity displayed by different current collector for AZIB anodes.

Anode	Current density and capacity	Cycle life	Reference
Zn @ Sn/Cu	0.5 mA cm^{-2}, 0.5 mAh cm^{-2}	250 h	[31]
Zn @ Cu mesh	1 mA cm^{-2}, 1 mAh cm^{-2}	180 h	[33]
ZnAl alloy @ Cu mesh	1 mA cm^{-2}, 0.25 mAh cm^{-2}	180 h	[37]
	0.5 mA cm^{-2}, 0.25 mAh cm^{-2}	230 h	
N-doped carbon fibers embedded with Cu nanoboxes	5 mA cm^{-2}, 2 mAh cm^{-2}	250 h	[38]
	2 mA cm^{-2}, 1 mAh cm^{-2}	450 h	
Zn @ Cu foam	2 mA cm^{-2}, 1 mAh cm^{-2}	150 h	[39]
Zn @ CNT	2 mA cm^{-2}, 2 mAh cm^{-2}	200 h	[40]
Zn @ MXene	5 mA cm^{-2}, 1 mAh cm^{-2}	300 h	[41]
Zn @ Cu$_2$Te flakes	1 mA cm^{-2}, 0.5 mAh cm^{-2}	400 h	This work
	5 mA cm^{-2}, 0.5 mAh cm^{-2}	510 h	This work
	10 mA cm^{-2}, 1 mAh cm^{-2}	120 h	This work

Batteries & Supercaps

Research Article
doi.org/10.1002/batt.202300107

Chemistry Europe
European Chemical
Societies Publishing

Encouraged by the excellent electrochemical performance of Zn@δ-CTFs symmetric cells, the anode of Zn@δ-CTFs was assembled with δ-MnO$_2$ into full cells (denoted as Zn@δ-CTFs//MnO$_2$) to demonstrate the pratical usage. The cyclic voltammetry (CV) measurement was conducted at the scan rate of 0.1 mV s^{-1} from 0.1 V to 1.8 V. The profiles of the first three cycles were recorded as Figure 5(a). The first CV curve exhibited one cathodic peak located at 1.21 V and one anodic peak located at 1.56 V, which was abscribed to the insertsion/extraction of Zn^{2+} into/out of MnO$_2$.[29] In addition, the 2nd and 3rd CV sweeping profiles exhibited a new anodic peak and cathodic peak where located at the 1.66 V and 1.36 V, respectively, which infered to the insertion of Zn^{2+} and H$^+$. Figure 5(b) displayed the rate-dependent capacity of Zn@δ-CTFs//MnO$_2$ and Zn@Cu//MnO$_2$ at various current densities ranging from 0.5 to 5 A g^{-1}. The full cell of Zn@δ-CTFs//MnO$_2$ exhibits high discharge capacities of 198, 130, 80, and 45 mAh g^{-1} at current densities of 0.5, 1.0, 2.0, and 5.0 A g^{-1}, which were superior to that of Zn@Cu//MnO$_2$. Next, during the charge/discharge process, the Zn striping/plating cyclically

repeated on the electrode. Hence, the interfacial ion/electron transport at the electrode played a decisive role. To further invesitgate the charge transport at the interface between electrodes, electrochemistry impedance spectroscopy (EIS) was employed for Zn@Cu//MnO$_2$ and Zn@δ-CTFs//MnO$_2$, respectively. Figure 5(c) displayed the results of EIS curves for Zn@Cu//MnO$_2$ (blue dots) and Zn@δ-CTFs//MnO$_2$ (red dots), respectively, exhibiting the charge transfer resistance (R$_{ct}$) of Zn@δ-CTFs//MnO$_2$ was lower than that of Zn@Cu//MnO$_2$, which was ascribed to the increased surface area by constructing 3D structures (standing 2D flakes), high ionic/electrical conductivity[45] and the zincophilic nature of Cu$_2$Te. In the Figure 5(d), our Zn@δ-CTFs//MnO$_2$ full batteries successfully powered the red-light led. The cycling performance of Zn@δ-CTFs//MnO$_2$, Zn@Cu//MnO$_2$ and Zn//MnO$_2$ full batteries were examined at the current density of 1 A g^{-1}. For the performance of the Zn@Cu//MnO$_2$, the abrupt degradation of capacity around 380 cycles was observed, which was attributed to the dendrite formation, resulting in the internal short curcuit. Moreover, it was also speculated that MnO$_2$ was partially
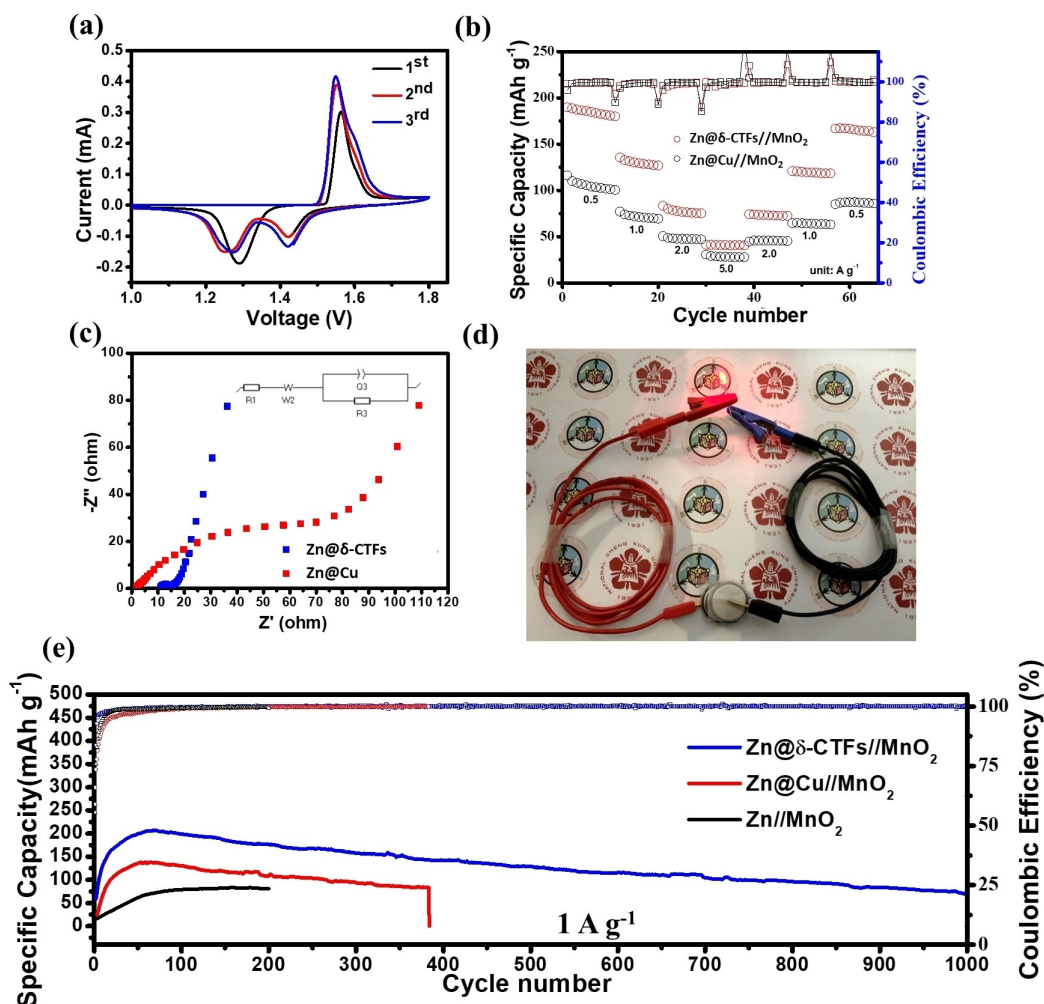
Figure 5. Electrochemical results of Zn@δ-CTFs//MnO$_2$ full batteries. a) The first three CV curves of Zn@δ-CTFs//MnO$_2$ full batteries. b) Rate-dependent capacity followed by the rate of 0.5, 1, 2 and 5 A g^{-1}. c) EIS spectra of Zn@δ-CTFs//MnO$_2$ (blue line), Zn@Cu//MnO$_2$ (red line). d) Photograph of Zn@δ-CTFs//MnO$_2$ coin cell, driving the red-light led. e) Cycling stability test of Zn@δ-CTFs//MnO$_2$ (blue line), Zn@Cu//MnO$_2$ (red line) and Zn//MnO$_2$ (black line) full batteries, respectively.

Batteries & Supercaps

Research Article
doi.org/10.1002/batt.202300107

Chemistry Europe
European Chemical
Societies Publishing

dissolved into the acid electrolyte, resulting in the capacity decay, which had been confirmed the notorious fact existing in MnO_2.[46] Hence, the development of suitable cathode for AZIB toward the long-term rigidity of structure during Zn ions insertion/extraction still remained challenged. Moreover, it was worth noting that the capacity of Zn@δ-CTFs//MnO_2 increased in the first 100 cycles (Figure S10), and reasonably speculated that during the Zn striping/plating process, the active materials gradually achieved the uniform distribution, resulting in the acceleration of the kinetics. The activation process was similar to what commonly observed in the Li/S batteries.[47] Remarkably, our Zn@δ-CTFs//MnO_2 full batteries delivered the higher initial capacity of 214 mAh cm^{-2} which was attributed to the lower R_{ct} and retained 100 mAh cm^{-2} after 1000 cycling (Figure 5e), exhibiting the effective suppression of dendrite formation during Zn ions plating/striping.

To confirm the surface stability of Zn@δ-CTFs anode after cycling, an *ex-situ* SEM observation was performed. The full cell of Zn@Cu//MnO_2 and Zn@δ-CTFs //MnO_2 were disassembled at various cycling numbers. First, the surface of the Zn@Cu anode showed vigorous growth of dendritic structures after 100 cycles at 1 A g^{-1}, and further magnified revealing the formation of hexagonal flakes, confirmed the Zn dendrites formation (Figure 6a1 and a2). On contrary, the surfce of Zn@δ-CTFs anode apparently covered with lace-like films without the dendritic structure after 1000 cycles at 5 A g^{-1} (Figure 6b1). Even at 1 A g^{-1} after 1000 cycles, the standing flakes were still observed, but were completely covered with lace-like films (Figure 6b2). Subsequently, the results of the compositional mapping analysis conducted by SEM-EDX exhibited the distribution of Cu, Zn and Te, which perfectly reflected the flakes structure, confirmed the Zn stripping/plating process were governed by the 3D structure of δ-CTFs (Figure 6c1–c4). In addition, X-ray analysis was conducted for Zn@Cu and Zn@δ-CTFs after cycling

at different cycles (Figure S11). Obviously, the peaks of by-products $Zn_4SO_4(OH)_6 \cdot 5H_2O$ was detected for Zn@Cu after cycling. In contrast, as for Zn@δ-CTFs, the peaks of byproducts were not detected even after 48 cycles, exhibited effective suppression of Zn dendrites. The above results indicated that the δ-CTFs as the current collector is the potential alternatives due to the synergistic effect of the zincophilicity and 3D structure, resulting in substantially superior surface stability.

Conclusions

In summary, this study discovers a new kind of zincophilic 2D materials, δ-CTFs which was successfully synthesized through the post-tellurization of Cu foil. It was discovered that the resulting morphology of δ-CTFs were sensitive to the parameter tuning from 2D flakes to thin film growth. The (002) plane of δ-CTFs grew epitaxially on the (111) plane of Cu, resulting in the vertical 3D structure. Through the characteristic analysis by XRD, XPS and TEM, the crystallinity as well as atomic structure were identified, proving the high crystallinity and δ phase synthesized at 400 °C. By comparison, the post-tellurization process developed in this research guaranteed the larger area growth with time-saving approach. Next, δ-CTFs were exploited as current collect to electrodeposit the Zn as anode, exhibited the ultralow nucleation overpotential (7.0 mV) and excellent hydrophilicity. More interestingly, the electrodeposited Zn was guided to laterally deposit on the (002) plane of standing δ-CTFs, effectively suppressed the preferred deposition toward Z-axis direction. Importantly, the symmetry cell displayed the long-term stability up to 400 hr, much longer than that of using bare Cu as the current collector. Finally, Zn@δ-CTFs was coupled with the commonly used MnO_2 as cathode for the full cell demonstration, presenting the 100% CE with keeping the
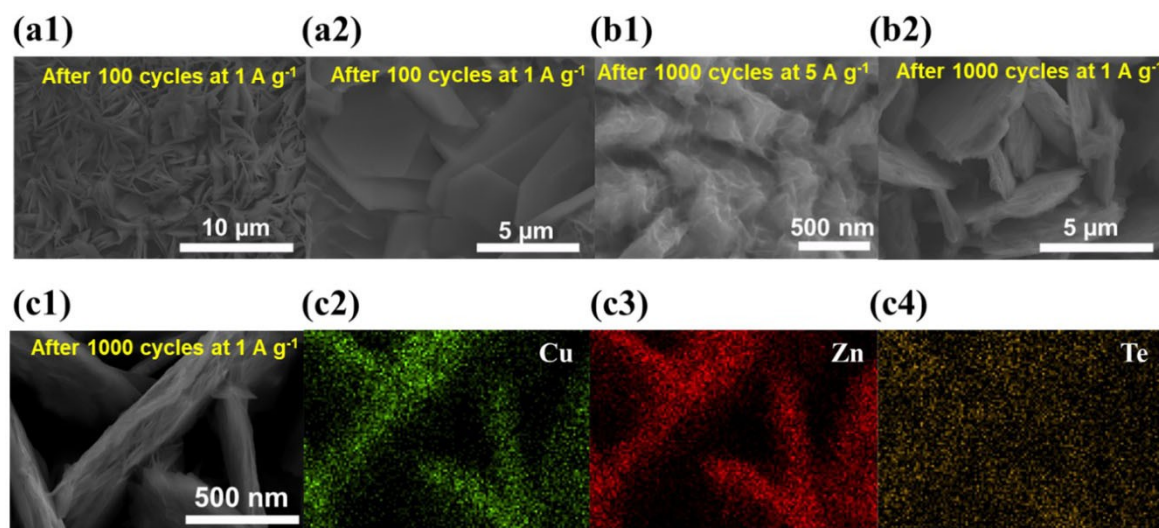
Figure 6. SEM images of Zn@Cu anode a1) after 100 cycles at 1 A g^{-1}, and a2) the magnified image of Zn dendrites, revealing the hexagonal flakes. b1) SEM images of Zn@δ-Cu_2Te anode (a1) after 1000 cycles at 5 A g^{-1}, and a2) after 1000 cycles at 1 A g^{-1}, confirming no dendritic structure formed at the surface. c1) Magnified image of Zn@δ-Cu_2Te anode and the corresponding SEM-EDS mapping of c2) Cu element, c3) Zn element and c4) Te element, respectively, proving Zn stripping/plating process were guided by the 3D structure of standing Cu_2Te flakes, effectively suppressed the Zn dendrites.

Batteries & Supercaps

Research Article
doi.org/10.1002/batt.202300107

Chemistry Europe
European Chemical
Societies Publishing

capacity of 100 mAh g^{-1} over 1000 cycles. Meanwhile, the Zn distribution after charge/discharge process were regulated along the standing δ-CTFs without the formation of Zn dendrite. This work provided a facile approach to synergize the 2D materials Cu$_2$Te with 3D structure for the long-term dendrite-free anode.

Experimental Section

Synthesis of δ-Cu₂Te flakes by the post-tellurization process

δ-Cu$_2$Te flakes (δ-CTFs) on Cu foil was synthesized using the following procedure. At first, Cu foil (Thermo Scientific) was cut into 16 mm circle and emerged in ethanol for 15 min and then 0.5 M HCl for 5 min, respectively, then cleaned by DI water. δ-CTFs synthesized via the post-tellurization process were conducted in a horizontal furnace. A high purity Te powder (99%, Acros Organics) of 10 mg was put into quartz crucibles and placed in the upstream where is 10 cm away from the Cu foil substrate placed in the downstream. First, the horizontal furnace was heated to 900 °C for 60 min to purify the atmosphere in the tube. A mixture of Ar/H$_2$ with the ratio of 20/5 sccm were introduced under 10 torr and maintained to 400 °C for 30 min. After the growth process, the furnace was cooled down by fan to room temperature.

Preparation of aqueous zinc-ion battery (AZIB)

A coin cell (CR-2032) was assembled by the following procedures. Firstly, Zn was deposited on δ-CTFs (Zn@δ-CTFs) by the electro-deposition method of using 1 M ZnSO$_4$ and 0.5 M Na$_2$SO$_4$ as electrolyte at the current density of 10 mA cm^{-2} for 30 min by PGSTAT30 (Metrohm Auto lab) electrochemical instrument.

For the synthesis of δ-MnO$_2$ as cathode, the precursors of KMnO$_4$ and MnSO$_4$ mixed with a molar ratio of 6:1 (totally 0.015 mol in 60 ml DI water) and then well-stirred for awhile. The resulting solution was put into an autoclave and heated to 160 °C maintained for 12 h and then naturally-cooled to room temperature. The resulting powders were further processed through the centrifuge, DI-water washed and followed by drying at 80 °C overnight. For the preparation of cathode, the mass loading of δ-MnO$_2$ was 2.5 mg and mixed with acetylene black, and polytetrafluoroethylene (PTFE) by the mass ratio of 7:2:1 with the addition of ethonal. The resultant product was stirred for 24 h at room temperature and then coated on carbon paper uniformly. Finally, the δ-MnO$_2$-coated carbon paper cut into circle electrodes with diameter of 14 mm and followed by drying at 70 °C for 24 h in a vacuum oven. The Zn@δ-CTFs anodes with glass fiber as the seperator and dropwised with 2 M ZnSO$_4$ until completely soaked and subsequently, assemble with δ-MnO$_2$-coated carbon paper as cathode into a full battery. All assembling procedures were performed in the air.

Material characterization

X-ray diffraction (XRD, D8 discover Bruker) with Cu–Kα radiation ($\lambda = 1.5418$ Å) was employed to verify the crystal structures by scanning from 20° to 60° with scan rate of 0.1 deg s^{-1}. Raman spectroscopy was exploited using LabRam HR 800 UV with 532 nm laser excitation. The morphology of the samples was characterized by field-emission scanning electron microscopy (FE-SEM, Hitachi, SU-5000) and high-resolution transmission electron microscopy (HR-TEM, JEM-2100F FEGTEM, JEOL). The sample of Cu$_2$Te for TEM observation was prepared by the focused ion beam System (FIB, Hitachi NX2000). The compositional analysis was investigated by energy dispersive spectroscopy (EDS) equipped in SEM. X-ray photoelectron spectroscopy (XPS, ULVAC-PHI, PHI 5000 Versa Probe) was performed for determining the chemical state of the elements of Te and Cu.

Electrochemical characterization

To investigate the electrochemical performance of CR2032, cyclic voltammetry (CV) and galvanostatic charge/discharge measurements were evaluated by using a PGSTAT30 (Metrohm Auto lab) electrochemical instrument at room temperature. The CV measurement swept from 0 to 1.8 V at the scan rate 0.1 mV s^{-1}. The electrochemical impedance spectroscopy (EIS) was measured with a frequency range from 10^5 Hz to 10^{-2} Hz. The galvanostatic charge/discharge (GCD) was performed in the voltage range of 0.8 to 1.8 V by CT-4008.

Supporting Information

Supporting Information is available from the Wiley Online Library or from the author. Additional references cited within the Supporting Information.[48–51]

Conflict of Interests

The authors declare no competing financial interest.

Data Availability Statement

The data that support the findings of this study are available from the corresponding author upon reasonable request.

[1] W. Li, B. Song, A. Manthiram, *Chem. Soc. Rev.* **2017**, *46*, 3006.
[2] D. Chao, W. Zhou, F. Xie, C. Ye, H. Li, M. Jaroniec, S.-Z. Qiao, *Sci. Adv.* **2020**, *6*, eaba4098.
[3] B. Tang, L. Shan, S. Liang, J. Zhou, *Energy Environ. Sci.* **2019**, *12*, 3288.
[4] Z. Chen, Q. Yang, F. Mo, N. Li, G. Liang, X. Li, Z. Huang, D. Wang, W. Huang, J. Fan, C. Zhi, *Adv. Mater.* **2020**, *32*, 2001469.

Batteries & Supercaps

Research Article
doi.org/10.1002/batt.202300107

Chemistry Europe
European Chemical
Societies Publishing

[5] Q. Yang, Q. Li, Z. Liu, D. Wang, Y. Guo, X. Li, Y. Tang, H. Li, B. Dong, C. Zhi, *Adv. Mater.* **2020**, *32*, 2001854.

[6] W. Lu, C. Xie, H. Zhang, X. Li, *ChemSusChem* **2018**, *11*, 3996.

[7] F. R. McLarnon, E. J. Cairns, *J. Electrochem. Soc.* **1991**, *138*, 645.

[8] L. F. Arenas, A. Loh, D. P. Trudgeon, X. Li, C. Ponce de León, F. C. Walsh, *Renewable Sustainable Energy Rev.* **2018**, *90*, 992.

[9] Q. Jian, T. Wang, J. Sun, M. Wu, T. Zhao, *Energy Storage Mater.* **2022**, *53*, 559.

[10] R. Yuksel, O. Buyukcakir, W. K. Seong, R. S. Ruoff, *Adv. Energy Mater.* **2020**, *10*, 1904215.

[11] Y. An, Y. Tian, K. Zhang, Y. Liu, C. Liu, S. Xiong, J. Feng, Y. Qian, *Adv. Funct. Mater.* **2021**, *31*, 2101886.

[12] L. Ma, Q. Li, Y. Ying, F. Ma, S. Chen, Y. Li, H. Huang, C. Zhi, *Adv. Mater.* **2021**, *33*, 2007406.

[13] Y. Yang, C. Liu, Z. Lv, H. Yang, Y. Zhang, M. Ye, L. Chen, J. Zhao, C. C. Li, *Adv. Mater.* **2021**, *33*, 2007388.

[14] S. D. Pu, C. Gong, Y. T. Tang, Z. Ning, J. Liu, S. Zhang, Y. Yuan, D. Melvin, S. Yang, L. Pi, J.-J. Marie, B. Hu, M. Jenkins, Z. Li, B. Liu, S. C. E. Tsang, T. J. Marrow, R. C. Reed, X. Gao, P. G. Bruce, A. W. Robertson, *Adv. Mater.* **2022**, *34*, 2202552.

[15] Z. Chen, J. Zhao, Q. He, M. Li, S. Feng, Y. Wang, D. Yuan, J. Chen, H. N. Alshareef, Y. Ma, *ACS Energy Lett.* **2022**, *7*, 3564.

[16] Z. Cao, P. Zhuang, X. Zhang, M. Ye, J. Shen, P. M. Ajayan, *Adv. Energy Mater.* **2020**, *10*, 2001599.

[17] Z. Kang, C. L. Wu, L. B. Dong, W. B. Liu, J. Mou, J. W. Zhang, Z. W. Chang, B. Z. Jiang, G. X. Wang, F. Y. Kang, C. J. Xu, *ACS Sustainable Chem. Eng.* **2019**, *7*, 3364.

[18] Q. Jian, Z. Guo, L. Zhang, M. Wu, T. Zhao, *Chem. Eng. J.* **2021**, *425*, 130643.

[19] B. Liu, S. Wang, Z. Wang, H. Lei, Z. Chen, W. Mai, *Small* **2020**, *16*, 2001323.

[20] Y. Fang, Y. Luan, D. Chen, S. Gao, X. W. Lou, *Angew. Chem. Int. Ed.* **2020**, *59*, 7178.

[21] M. Ye, C. Chen, N. Zhang, X. Wen, W. Guo, C. Lin, *Adv. Energy Mater.* **2014**, *4*, 1301564.

[22] R. Nunna, P. Qiu, M. Yin, H. Chen, R. Hanus, Q. Song, T. Zhang, M.-Y. Chou, M. T. Agne, J. He, G. J. Snyder, X. Shi, L. Chen, *Energy Environ. Sci.* **2017**, *10*, 1928.

[23] K. Zhao, K. Liu, Z. Yue, Y. Wang, Q. Song, J. Li, M. Guan, Q. Xu, P. Qiu, H. Zhu, L. Chen, X. Shi, *Adv. Mater.* **2019**, *31*, 1903480.

[24] H. Sun, O. A. Zelekew, X. Chen, Y. Guo, D.-H. Kuo, Q. Lu, J. Lin, *RSC Adv.* **2019**, *9*, 31828.

[25] J. Liu, J. Zhang, *Chem. Rev.* **2020**, *120*, 2123.

[26] S. Mukherjee, R. Chetty, P. V. P. Madduri, A. K. Nayak, K. Wojciechowski, T. Ghosh, K. Chattopadhyay, S. Suwas, R. C. Mallik, *Dalton Trans.* **2019**, *48*, 1040.

[27] M. Liu, L. Yang, H. Liu, A. Amine, Q. Zhao, Y. Song, J. Yang, K. Wang, F. Pan, *ACS Appl. Mater. Interfaces* **2019**, *11*, 32046.

[28] S. S. Dhasade, S. H. Han, V. J. Fulari, *J. Semicond.* **2012**, *33*, 093002.

[29] C. Xu, B. Li, H. Du, F. Kang, *Angew. Chem. Int. Ed.* **2012**, *51*, 933.

[30] T.-C. Huang, K.-W. Cheng, C.-A. Lin, Y.-C. Fu, S.-K. Lin, Y.-Z. Chen, *Sustain. Energy Fuels* **2022**, *6*, 4626.

[31] Y. Huang, Z. Chang, W. Liu, W. Huang, L. Dong, F. Kang, C. Xu, *Chem. Eng. J.* **2022**, *431*, 133902.

[32] Y. Qian, C. Meng, J. He, X. Dong, *J. Power Sources* **2020**, *480*, 228871.

[33] Q. Zhang, J. Luan, L. Fu, S. Wu, Y. Tang, X. Ji, H. Wang, *Angew. Chem. Int. Ed.* **2019**, *58*, 15841.

[34] Y. Shang, P. Kumar, T. Musso, U. Mittal, Q. Du, X. Liang, D. Kundu, *Adv. Funct. Mater.* **2022**, *32*, 2200606.

[35] C. Li, X. Shi, S. Liang, X. Ma, M. Han, X. Wu, J. Zhou, *Chem. Eng. J.* **2020**, *379*, 122248.

[36] Y. Zeng, P. X. Sun, Z. Pei, Q. Jin, X. Zhang, L. Yu, X. W. Lou, *Adv. Mater.* **2022**, *34*, 2200342.

[37] Z. Qi, T. Xiong, T. Chen, C. Yu, M. Zhang, Y. Yang, Z. Deng, H. Xiao, W. S. V. Lee, J. Xue, *ACS Appl. Mater. Interfaces* **2021**, *13*, 28129.

[38] Y. X. Zeng, P. X. Sun, Z. H. Pei, Q. Jin, X. T. Zhang, L. Yu, X. W. Lou, *Adv. Mater.* **2022**, *34*, 2200342.

[39] C. P. Li, X. D. Shi, S. Q. Liang, X. M. Ma, M. M. Han, X. W. Wu, J. Zhou, *Chem. Eng. J.* **2020**, *379*, 122248.

[40] Y. Zeng, X. Zhang, R. Qin, X. Liu, P. Fang, D. Zheng, Y. Tong, X. Lu, *Adv. Mater.* **2019**, *31*, 1903675.

[41] Z. Gong, P. Wang, K. Ye, K. Zhu, J. Yan, G. Wang, G. Chen, D. Cao, *J. Colloid Interface Sci.* **2022**, *625*, 700.

[42] Z. Yao, Y. Lum, A. Johnston, L. M. Mejia-Mendoza, X. Zhou, Y. Wen, A. Aspuru-Guzik, E. H. Sargent, Z. W. Seh, *Nat. Rev. Mater.* **2022**, DOI: 10.1038/s41578-022-00490-5.

[43] K. N. Tu, Y. Liu, M. Li, *Appl. Phys. Rev.* **2017**, *4*, 011101.

[44] H. B. Huntington, A. R. Grone, *J. Phys. Chem. Solids* **1961**, *20*, 76.

[45] S. Mukherjee, R. Parasuraman, A. M. Umarji, G. Rogl, P. Rogl, K. Chattopadhyay, *J. Alloys Compd.* **2020**, *817*, 152729.

[46] J. Heo, S. Chong, S. Kim, R. Kim, K. Shin, J. Kim, H.-T. Kim, *Batteries & Supercaps* **2021**, *4*, 1881.

[47] S.-H. Chung, A. Manthiram, *Joule* **2018**, *2*, 710.

[48] Y.-c. Liu, B. Afflerbach, R. Jacobs, S.-k. Lin, D. Morgan, *MRS Commun.* **2019**, *9*, 567–575.

[49] R. Jacobs, T. Mayeshiba, B. Afflerbach, L. Miles, M. Williams, M. Turner, R. Finkel, D. Morgan, *Comput. Mater. Sci.* **2020**, *176*, 109544.

[50] F. Pedregosa, G. Varoquaux, A. Gramfort, V. Michel, B. Thirion, O. Grisel, M. Blondel, P. Prettenhofer, R. Weiss, V. Dubourg, J. Vanderplas, A. Passos, D. Cournapeau, M. Brucher, M. Perrot, É. Duchesnay, *J. Mach. Learn. Res.* **2011**, *12*, 2825.

[51] K. Zhao, K. Liu, Z. Yue, Y. Wang, Q. Song, J. Li, M. Guan, Q. Xu, P. Qiu, H. Zhu, *Adv. Mater.* **2019**, *31*, 1903480.